Photochemistry of organometallics: quantum chemistry and photodissociation dynamics

M.C. Heitz [a], K. Finger [b], C. Daniel [a,*]

[a] *Laboratoire de Chimie Quantique, UPR 139 du CNRS, Université Louis Pasteur,
4 Rue Blaise Pascal, F-67000 Strasbourg, France*
[b] *Institut für Physikalische und Theoretische Chemie, Freie Universität, D-14195 Berlin,
Germany*

Contents

---

* Corresponding author.

Abstract

The photodissociation dynamics of three model systems in the lowest electronically excited states, $HCo(CO)_4$, $H_2Fe(CO)_4$ and $HMn(CO)_3(\alpha$-diimine), each representative of a class of transition metal complexes, are reported for the following elementary processes: (i) ultrafast (within ca. 20 to 100 fs) direct dissociation on a single totally repulsive potential; (ii) ultrafast (within ca. 20 fs) dissociation on three kinetically coupled potentials; (iii) fast (within ca. 10 ps) indirect dissociation via tunneling through a potential energy barrier; (iv) indirect dissociation via fast (within ca. 10 ps) spin–orbit coupling induced intersystem crossing. By extension of the strategy applied with success to small di- and triatomic molecules to multidimensional transition metal complexes, the dynamics are simulated using a time-dependent wave packet propagation technique on ab initio CASSCF/CCI potential energy surfaces. The nature of the photoactive excited states is determined without ambiguity, as well as the time scales, the branching ratio of the primary reactions and some important features of the absorption spectra. An example of mode selective control of a unimolecular dissociation by a two-photon laser strategy is reported for $HCo(CO)_4$. © 1997 Elsevier Science S.A.

Keywords: Photodissociation dynamics; Organometallics

1. Introduction

The last decade has seen the expansion of sophisticated new laser experiments developed in connection with study of fast (picosecond) or ultra-fast (femtosecond) photoprocesses following the absorption of light. These new techniques, applied with success to small polyatomic molecules, are capable of selectively enhancing the rates of photodissociation or controlling the product branching ratio of competing bond breaking [1]. At the same time, exact quantum simulations of the photodissociation of triatomic molecules have been developed with the aim of connecting the nuclear motion on accurate multidimensional potential energy surfaces to the observables [2,3]. Despite this evolution, the application of quantum time-dependent wave packet propagation methods to large molecules in excited states is still a challenge. The photochemistry of organometallics represents a new and interesting field of investigation.

The conventional photochemistry of transition metal carbonyls has a wide variety of applications, such as production of catalytically active species, synthesis of substituted derivatives or spectroscopic investigations [4–6]. More recent multiphoton laser experiments have seen the development of new applications like the deposition of thin metal films, the generation of ground state metal atoms or neutral atomic precursors of selected states of metal ions [7]. The photochemistry of organometallic compounds with low-lying metal-to-ligand charge transfer (MLCT) states is mainly used to understand and reproduce photoenergy and electron transfer processes occurring in natural phenomena [8–10]. In classic experiments (long and monochromatic laser pulses), the UV–visible spectra are usually broad and featureless and detailed assignment is usually lacking. Sophisticated fast time-resolved infrared (TRIR) spectroscopy has been developed to follow the behavior of short lifetime intermediates [11].

However, according to recent pico-/femtosecond experiments reported on [CpFe(CO)$_2$]$_2$ [12], the major difficulty is to distinguish the early stage of the photodissociation (in the femtosecond time scale) from vibrational relaxation effects.

The exploration of the potential energy surfaces associated with the excited states contributing to the absorption/emission spectra and/or participating in the photodissociation, by the means of the time-dependent theory, represents a promising alternative for the understanding and the analysis of the sequence of events occurring between the initial excitation and the formation of the primary products.

In recent simulations, we extended the model proposed by Imre and coworkers [3] for competitive bond breaking from simple linear triatomic ABC systems

$$AB + C \leftarrow [ABC]^* \rightarrow A + BC \tag{1}$$

to large transition metal complexes. The complex network of elementary processes (intramolecular vibrational energy redistribution (IVR), intersystem crossing (ISC), internal conversion (IC), direct dissociation (DD) on repulsive potential energy surfaces (PES) in the femtosecond timescale or indirect dissociation (ID) after tunneling or IVR in the picosecond timescale) that govern the photochemistry of organometallics has been considered under the time-dependent approach for a series of model systems, each representative of a class of molecules [13–16]. The aim of the present contribution is to report the recent advances, based on quantum chemical calculations coupled with photodissociation dynamics, performed in the field of the photochemistry of organometallics. The model, techniques and properties directly related to the observables are explained briefly in Section 2. The results of the simulation by propagation of representative wavepackets on the PES, obtained from ab initio calculations and corresponding to the lowest excited states, are presented and discussed in Section 3, with a short conclusion in Section 4.

2. Model and techniques

2.1. Model systems

The choice of the model systems has been motivated by our preliminary studies based on the analysis of the potential energy curves (PECs) that connect the electronic ground and excited states of the reactant to those of the primary products. Qualitative mechanisms have been proposed for a number of organometallics which exhibit concurrent photochemical reactions (metal–hydrogen bond vs. CO loss (HCo(CO)$_4$, HMn(CO)$_5$) [17], elimination of molecular hydrogen vs. ligand loss (H$_2$Fe(CO)$_4$, H$_2$Os(CO)$_4$, H$_2$Os(CO)Mes) [18], metal–alkyl or metal–metal bond breaking vs. ligand loss (AlPR, P = Porphine anion, Mn$_2$(CO)$_{10}$) [19] upon irradiation, either at a unique wavelength or at different wavelengths. More recently, we have investigated the role of the low-lying MLCT excited states in transition metal (α-diimine) complexes on the basis of the PEC calculated for the breaking of the

metal–hydrogen bond and the departure of a carbonyl ligand in the model system $HMn(CO)_3(\alpha\text{-diimine})$ [20].

The photodissociation dynamics of transition metal hydrides has been analyzed on the basis of a model simulation reported for $HCo(CO)_4$ which undergoes two primary reactions upon irradiation at 254 nm [14]:

$$H + Co(CO)_4 \leftarrow \left[HCo(CO)_4 \right]^* \rightarrow CO + HCo(CO)_3 \tag{2}$$
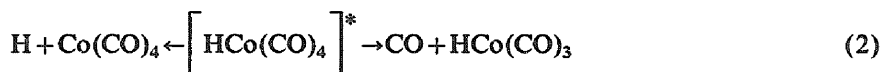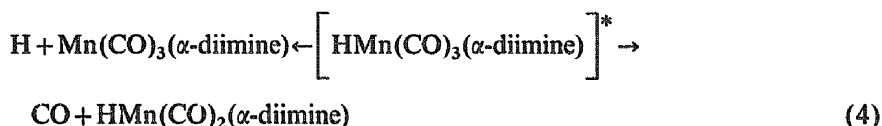
According to the experiments carried out by Sweany [21–23] using low-temperature matrix isolation techniques, if one assumes that neither the photolyzed CO nor the H atom return to the metal, the branching ratio for the two primary reactions is $[CO + HCo(CO_3)]/[H + Co(CO)_4] = 8:1$.

The photodissociation dynamics of transition metal dihydrides has been investigated for the model system $H_2Fe(CO)_4$ [24]:

$$H_2 + Fe(CO)_4 \leftarrow \left[H_2Fe(CO)_4 \right]^* \rightarrow CO + H_2Fe(CO)_3 \tag{3}$$
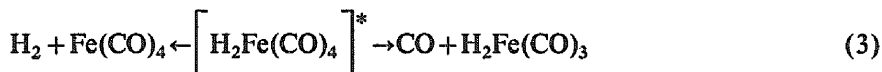
Evidence for the loss of dihydrogen from $H_2Fe(CO)_4$ has been reported from low-temperature matrix experiments [25] with no mention of carbonyl loss.

Finally, the photodissociation dynamics of transition metal complexes with low-lying MLCT excited has been simulated for the model system $HMn(CO)_3(\alpha\text{-diimine})$:

$$H + Mn(CO)_3(\alpha\text{-diimine}) \leftarrow \left[HMn(CO)_3(\alpha\text{-diimine}) \right]^* \rightarrow$$

$$CO + HMn(CO)_2(\alpha\text{-diimine}) \tag{4}$$

According to a number of experiments [26–34] reported for α-diimine mono- and di-nuclear transition metal carbonyls, it seems that these molecules may either behave like transition metal complexes without low-lying MLCT states, undergoing ligand dissociation or radical formation upon irradiation, or manifest the photophysics of MLCT complexes.

2.2. PESs

For the sake of simplicity, the molecules under investigation are modeled as pseudotriatomic molecules either with two collinear dissociative bonds, $q_a = [M\text{–}H]$ and $q_b = [M\text{–}CO_{ax}]$ for $HCo(CO)_4$ and $HMn(CO)_3(\alpha\text{-diimine})$, or with two noncollinear dissociative bonds, $q_a = [H_2\text{–}M]$ and $q_b = [M\text{–}CO]$ for $H_2Fe(CO)_4$. All other spectator modes are decoupled in this zero-order approximation. This decoupling mode should be reasonable, at least for ultrafast time scales (a few hundred femtoseconds) when initial energy remains stored in the dissociative bond(s). The relevant Hamiltonian is thus

$$H_e = T + V_e \tag{5}$$

depending on the electronic state e, with

$$T = p_a^2/2\mu_a + p_b^2/2\mu_b + p_a p_b/m_M \tag{6}$$

where p_a, p_b are the momenta conjugate to q_a, q_b and μ_a, μ_b are the corresponding reduced masses. Similar simplistic low-dimensional Hamiltonians have been employed previously for simulating the photodissociation of other pseudotriatomic systems [35], as starting models for more sophisticated studies.

It has been assumed that the C_{3v} symmetry is retained along the reaction paths corresponding to the photodissociation of $HCo(CO)_4$ (Eq. (2)) (Scheme 1), while the C_{2v} (elimination of H_2) or the C_s (CO loss) symmetries are conserved along the reaction pathways describing the photodissociation of $H_2Fe(CO)_4$ (Eq. (3)) (Scheme 2).
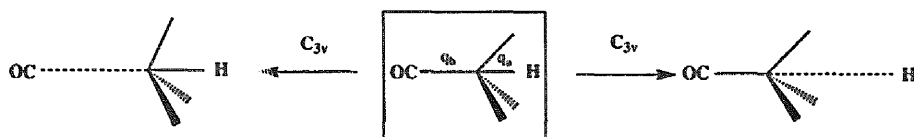
Scheme 1.
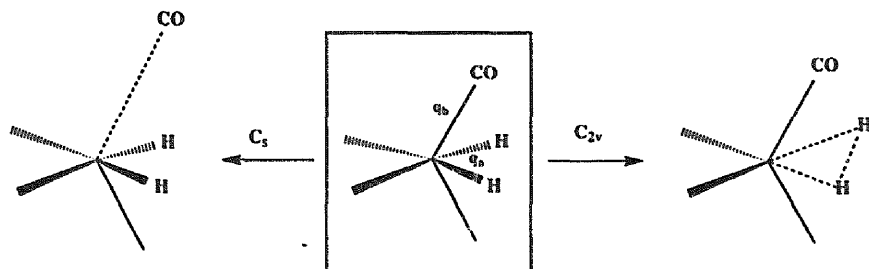
Scheme 2.
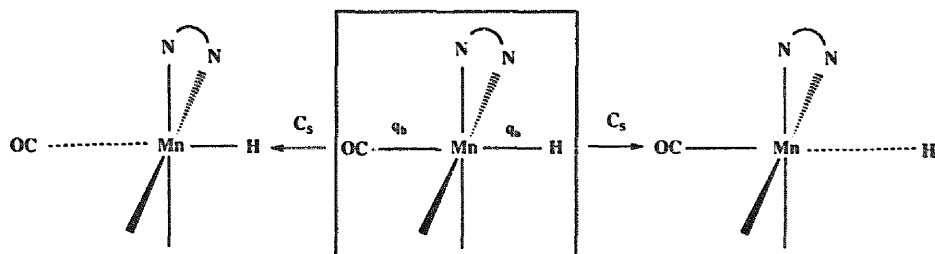
The photodissociation of $HMn(CO)_3(\alpha$-diimine$)$ (Eq. (4)) has been studied under C_s symmetry constraint (Scheme 3).

The PESs corresponding to the electronic ground states and the lowest excited

Scheme 3.

states of the model molecules are modeled by fitting analytical functions to CASSCF/CCI ab initio points, with additional smoothing to avoid any obvious artefact, such as shallow minima in the asymptotic domain. Details of the ab initio calculations (basis sets, size of the CI, CASSCF reference wavefunctions) are detailed elsewhere [13,15,16,20,29]. The choice of the electronic states selected for simulating the dynamics is governed by the preliminary studies based on state correlation diagrams and PECs calculated for the concurrent dissociation channels [17,18,20]. The first step of the simulation is the building of the theoretical absorption/emission spectra that need the PES corresponding to the electronic ground state and to the lowest singlet excited states directly accessible through spin- and symmetry-allowed transitions. The investigation of the photodissociation dynamics is based on potentials corresponding to dissociative electronic states (singlet and triplet).

2.3. Photodissociation dynamics

The photoabsorption and the subsequent competing bond breaking described in the reactions of Eqs. (2)–(4) are simulated by propagation of selected wavepackets:

$$\left\langle q_a, q_b \middle| \Psi_e(t) \right\rangle = \Psi(q_a, q_b, t) \tag{7a}$$

with

$$\Psi_e(q_a, q_b, t) = \exp(-iH_e t/\hbar) \Psi_e(q_a, q_b, t=0) \tag{7b}$$

on the different excited PESs.

For convenience, the corresponding wavepackets $\Psi_e(q_a, q_b, t)$ are also labeled by the initial quantum numbers v_a, v_b:

$$\Psi_e(q_a, q_b, t=0) = \left\langle q_a, q_b \middle| v_a, v_b \right\rangle_e \tag{8}$$

For the sake of simplicity, we will use the following short notation $|v_a, v_b\rangle$ in this report. In the applications reported in the next section, we restrict the propagation to a limited number of different initial wavepackets. The choice of the initial wavepackets is governed by the photophysics of the system under investigation: (i) in the simulation of a single photon absorption $v_a = v_b = 0$; (ii) in order to simulate selective investment of energy into reactants, we assume that the initially populated electronic excited state is prepared by IR+UV two photons absorption of the electronic ground state molecules [36], the IR photon serving to excite the electronic ground state into vibrational states with essentially v_a and v_b quanta in the modes q_a and q_b noted $|v_a, v_b\rangle_{a_e}$.

The wave packet $\Psi_e(q_a, q_b)$ is adapted from Refs. [37,38] when e is the electronic ground state, whereas it is evaluated by the Chebychev relaxation method [38] when

e is an electronic excited state. The time evolution of the wavepackets $\Psi_e(q_a, q_b, t)$ is evaluated by solving the time-dependent Schrödinger equation:

$$i\hbar \dot{\Psi}_e(q_a, q_b, t) = H_e \Psi_e(q_a, q_b, t) \tag{9}$$

by the fast Fourier transform (FFT) method [39]. The propagations are based on representations of $\Psi_e(q_a, q_b, t)$ on grids $q_{a_i} = q_{a_0} + i \cdot \Delta q_a, q_{b_j} = q_{b_0} + j \cdot \Delta q_b, t_k = k \cdot \Delta t$ with the parameters defined in Refs. [14,24,40]. The time evolution $\Psi_e(q_a, q_b, t)$ is illustrated by corresponding movies of the densities:

$$\rho_e(q_a, q_b, t) = \left| \Psi_e(q_a, q_b, t) \right|^2 \tag{10}$$

When the spin–orbit interaction between two electronic states k and k', defined by the spin–orbit coupling diabatic matrix element

$$V_{kk'}^d = \left\langle \Xi_k^{el} \left| \hat{H}_{SO} \right| \Xi_{k'}^{el} \right\rangle \tag{11}$$

is included for the description of singlet to triplet radiationless transitions, the time evolution of the wavepackets $\Psi_k(q_1, t)$ ($q_1 = q_a$ or q_b) in the diabatic representation is evaluated by solving a set of coupled time-dependent Schrödinger equations [41]:

$$i\hbar \Psi_k(q_1, t) = H_k \Psi_k(q_1, t) + \sum_{k \neq k'} V_{kk'}^d \Psi_{k'} \tag{12}$$

with specific initial conditions and a constant value for the spin–orbit coupling potential calculated, using the effective one-electron operator, on the basis of a restricted full CI scheme as described in detail in Ref. [42].

When several potentials are coupled nonadiabatically (symmetry avoided crossings), the time evolution of the wave packet $\Psi_k(q_1, t)$ ($q_1 = q_a$ or q_b) in the diabatic representation is obtained by solving the set of coupled time-dependent Schrödinger equations (Eq. (12)), where $V_{kk'}^d$ are the diabatic potential couplings obtained by a unitary transformation which shifts the kinetic couplings of the adiabatic representation into the potential matrix [43]. The kinetic couplings are sharply peaked around the avoided crossings regions and are approximated by asymmetric Lorentzians [43,44].

2.3.1. Properties

Several techniques are used to analyze the resulting wavepackets $\Psi_e(q_a, q_b, t)$ and to derive various properties useful for comparisons with experimental data and predictions for future sophisticated experiments, namely the movies of the densities, the branching ratio when two competing products channels are open on a given electronic state, the autocorrelation functions, and the emission/absorption spectra. The detail of these techniques is described elsewhere [13–16].

3. Results and discussion

3.1. Movies of the densities and time scale of direct dissociation

3.1.1. Photodissociation of $HCo(CO)_4$ ($^3A_1$ $\sigma \rightarrow \sigma^*$)

The time evolution of $HCo(CO)_4$ molecules in the $^3A_1$ excited state corresponding to the $\sigma \rightarrow \sigma^*$ excitation (σ and σ^* being the bonding and antibonding orbitals at the level of the Co–H bond respectively) starting from the initial state $\Psi_{^3A_1}(q_a,q_b,0) = |0,0\rangle_{^1E}$ is simulated by the time-dependent wave packet $\Psi_{^3A_1}(q_a,q_b,t)$ ($q_a = $[Co–H], $q_b = $[Co–CO$_{ax}$]) illustrated by snapshots of its density in Fig. 1.

The $V_{^3A_1}$ PES has a single exit valley corresponding to the Co–H bond homolysis; therefore, the entire wave packet $\Psi_{^3A_1}(q_a,q_b,t)$ runs out toward the primary products
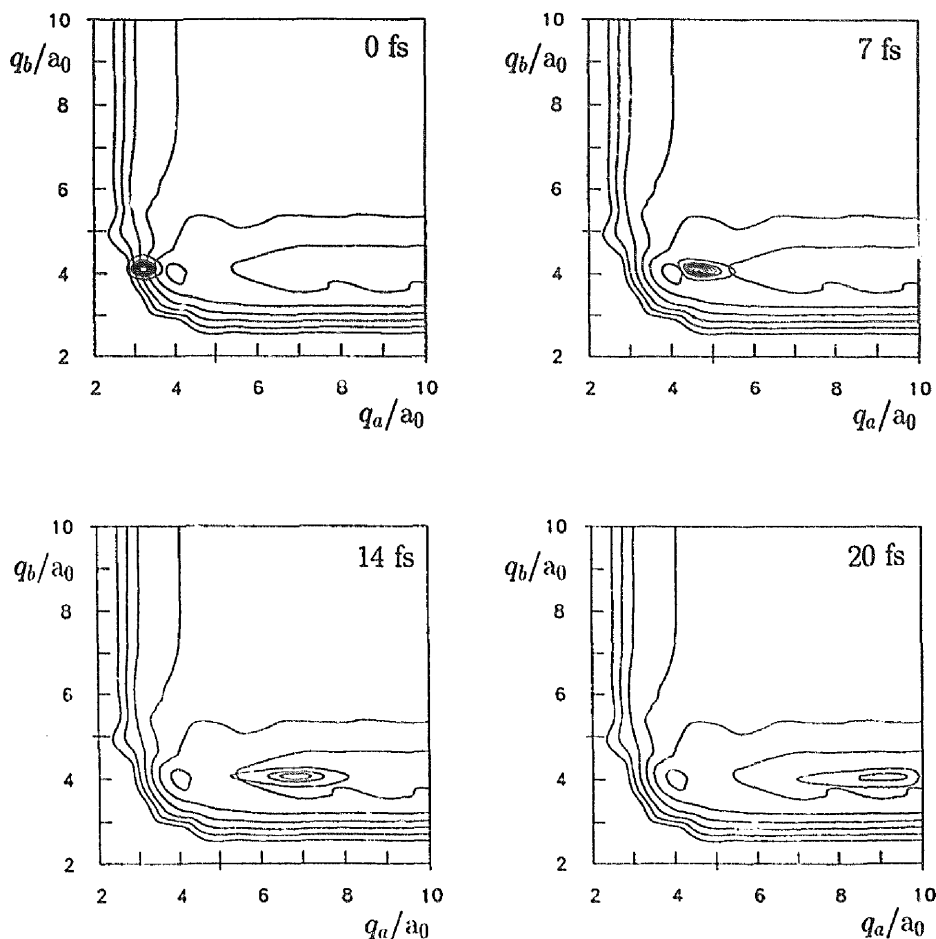

Fig. 1. Time evolution of the $\Psi_{^3A_1}(q_a,q_b,t)$ wave packet on the $V_{^3A_1}(q_a,q_b)$ PES of HCo(CO)$_4$($^3A_1$), from the initial state $\Psi_{^3A_1}(q_a,q_b,0 = |0,0\rangle_{^1E}$ prepared by $^1E \rightarrow {}^3A_1$ ISC [14].

$H + Co(CO)_4$ in their ground states. An ultrafast decay (within ca. 20 fs) characterized this DD occurring after $^1E \rightarrow {}^3A_1$ ISC.

3.1.2. Photodissociation of $H_2Fe(CO)_4$ (b^1A_1)

The time evolution of $H_2Fe(CO)_4$ molecules in the b^1A_1 excited state corresponding to a $d \rightarrow \sigma_g^*$ excitation (σ_g^* being the antibonding orbital between the iron atom and the bonding combination of the two hydrogen atoms) starting from the initial state $\Psi_{b^1A_1}(q_a, q_b, 0) = |0,0\rangle_{a^1A_1}$ and simulated by the time-dependent wave packet $\Psi_{b^1A_1}(q_a, q_b, t)$ ($q_a = [Fe-H_2]$, $q_b = [Fe-CO]$) is illustrated by snapshots of its density in Fig. 2.

This potential is selectively and entirely dissociative for the elimination of molecular hydrogen in an ultrafast process (within ca. 40 fs).
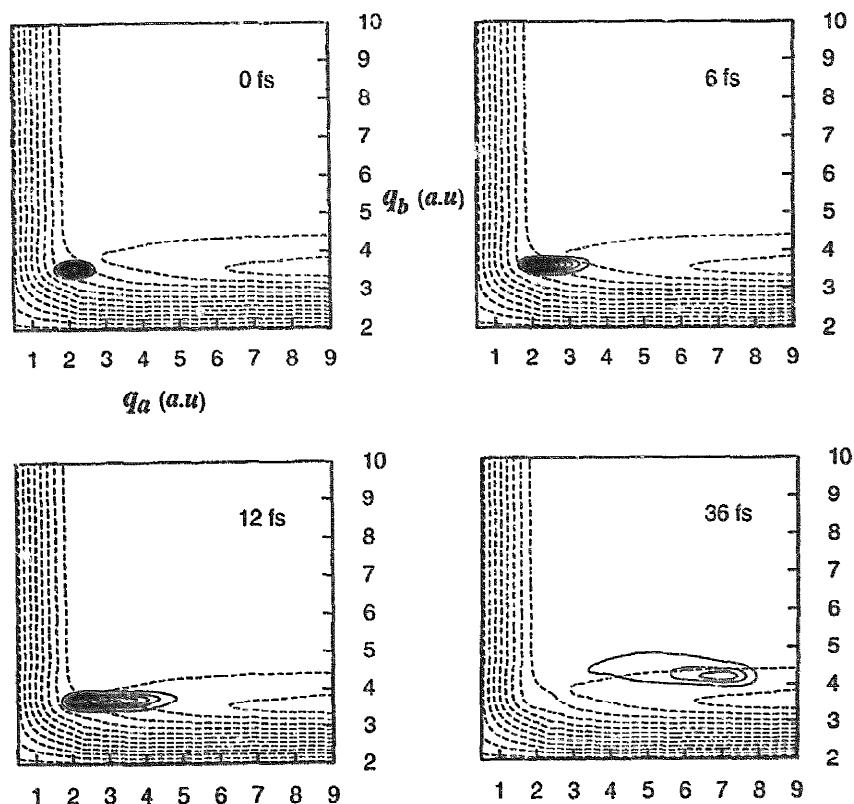

Fig. 2. Time evolution of the $\Psi_{b^1A_1}(q_a, q_b, t)$ wave packet on the $V_{b^1A_1}(q_a, q_b)$ PES of $H_2Fe(CO)_4(b^1A_1)$, from the initial state $\Psi_{b^1A_1}(q_a, q_b, 0) = |0,0\rangle_{a^1A_1}$ prepared by absorption $a^1A_1 \rightarrow b^1A_1$ [24].

3.2. Branching ratio of concurrent primary reactions on a single PES

3.2.1. Photodissociation of $HCo(CO)_4$ ($^1E\,d\rightarrow\sigma^*$)

The time evolution of the $\Psi_{^1E}(q_a,q_b,t)$ ($q_a = [Co–H]$, $q_b = [Co–CO_{ax}]$) wave packet on the ^1E potential characterized by a low energy barrier along the Co–H elongation, is illustrated in Fig. 3 by snapshots of the density $\rho_{^1E}(q_a,q_b,t)$ (Eq. (10)). The initial rather compact wavefunction $\Psi_{^1E}(q_a,q_b,t=0)=|0,0\rangle_{^1A_1}$ is split into two parts, α and β, representing dissociation into the primary products $H + Co(CO)_4$ in the ^1E excited state, and the IVR of the nondissociative $HCo(CO)_4(^1E)$ molecules get trapped in the potential well of the ^1E state.

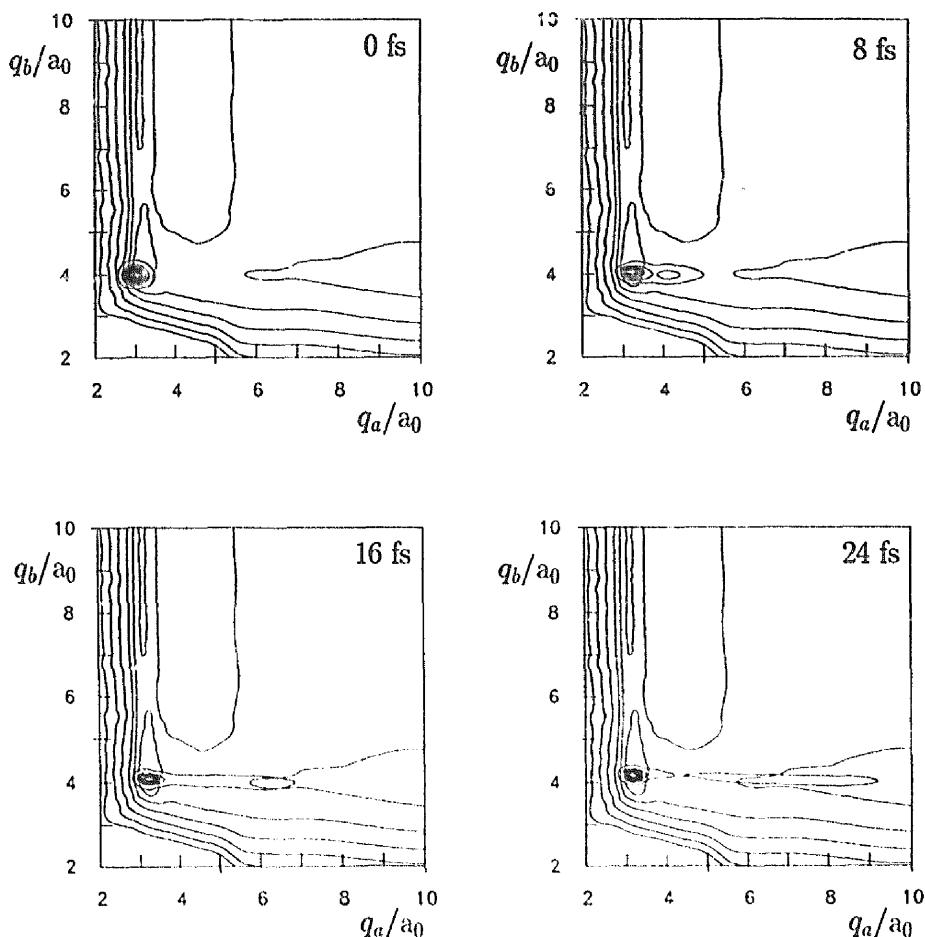The 'femtochemical' branching ratio gives $[H + Co(CO)_4]/[HCo(CO)_4(^1E,IVR)] \cong 0.35/0.65$. From the autocorrelation function shown in

Fig. 3. Time evolution of the $\Psi_{^1E}(q_a,q_b,t)$ wave packet on the $V_{^1E}(q_a,q_b)$ PES of $HCo(CO)_4(^1E)$, from the initial state $\Psi_{^1E}(q_a,q_b,0)=|0,0\rangle_{^1A_1}$ prepared by absorption $^1A_1\rightarrow{}^1E$ [14].
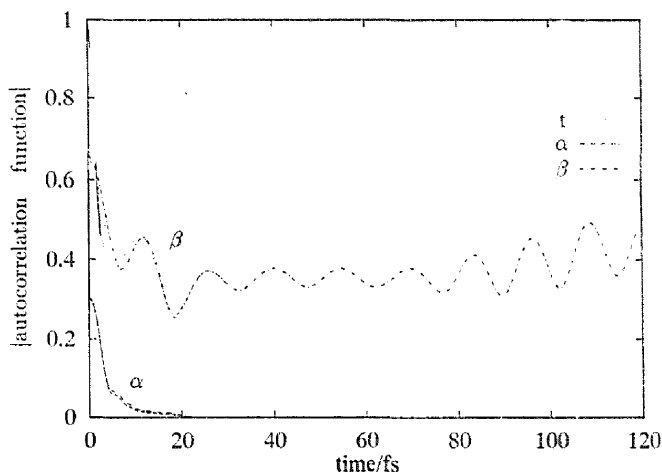
Fig. 4. Absolute values of the total (t) autocorrelation function $\langle \Psi_{^1E}(t=0)|\Psi_{^1E}(t)\rangle$ with contributions for products channels α (dissociation towards $H+Co(CO)_4(^1E)$) and β (IVR of $HCo(CO)_4(^1E)$) vs. time [14].

Fig. 4, one notices the ultrafast (ca. 5 fs) initial decay, which is caused by about equal contributions from both channels α and β. At later time $t \geq 10$ fs, one observes oscillatory recurrences, mainly due to the $Co-CO_{ax}$ vibrations which are the dominant accepting mode of the IVR channel β.

3.2.2. Photodissociation of $H_2Fe(CO)_4$ $(a^1B_1\ d\rightarrow\sigma_g^*)$

The time evolution of $H_2Fe(CO)_4$ molecules in the a^1B_1 excited state corresponding to a $d\rightarrow\sigma_g^*$ excitation (σ_g^* being the antibonding orbital between the iron atom and the bonding combination of the two hydrogen atoms) starting from the initial state $\Psi_{a^1B_1}(q_a,q_b,0)=|0,0\rangle_{a^1A_1}$ and simulated by the time-dependent wave packet $\Psi_{a^1B_1}(q_a,q_b,t)$ ($q_a=[Fe-H_2]$, $q_b=[Fe-CO]$) is illustrated by snapshots of its density in Fig. 5.

In an ultrashort time scale (ca. 20 fs) the wave packet dissociates towards the H_2 photoelimination primary products $[H_2+Fe(CO)_4.]$ After 30 fs, the wave packet is split into two parts α and β, 95% leading to the elimination of H_2, 5% dissociating along the channel corresponding to the carbonyl elimination within ca. 100 fs.

3.3. Fast predissociation via tunneling through a potential energy barrier

The $V_{a^1B_2}(q_a,q_b)$ potential ($q_a=[Fe-H_2]$, $q_b=[Fe-CO]$) corresponding to the $d\rightarrow\sigma_u^*$ excitation (σ_u^* being the antibonding orbital between the iron atom and the antibonding combination of the two hydrogen atoms) exhibits a potential energy barrier of the order of 10.0 kcal mol^{-1} at the early stage of the reaction path along the $Fe-H_2$ elongation ($q_a=2.57$ a.u. or 1.36 Å). The time evolution of the initial
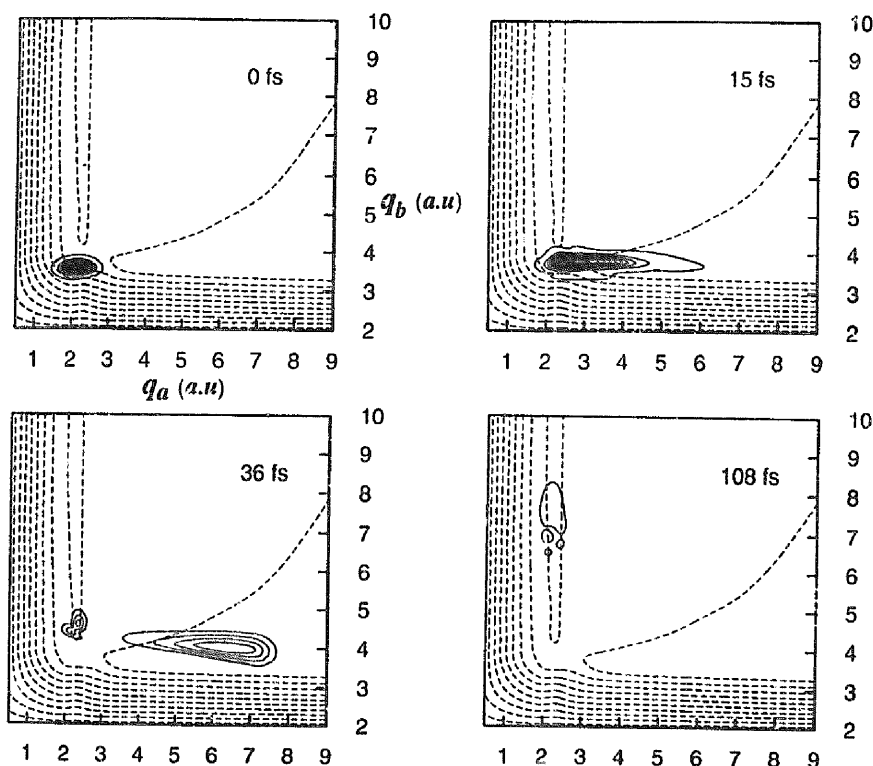
Fig. 5. Time evolution of the $\Psi_{a^1B_1}(q_a,q_b,t)$ wave packet on the $V_{a^1B_1}(q_a,q_b)$ PES of $H_2Fe(CO)_4(a^1B_1)$, from the initial state $\Psi_{a^1B_1}(q_a,q_b,0)=|0,0\rangle_{a^1A_1}$ prepared by absorption $a^1A_1\rightarrow a^1B_1$ [24].

state $\Psi_{a^1B_2}(q_a,q_b,0)=|0,0\rangle_{a^1A_1}$ is simulated by the time-dependent wave packet $\Psi_{a^1B_2}(q_a,q_b,t)$ and illustrated by snapshots of its density in Fig. 6.

There is no significant ultrafast DD, nearly 100% of the initial wave packet getting trapped into the potential well of the $V_{a^1B_2}(q_a,q_b)$ potential which coincides with the Franck–Condon region. Within ca. 1 ps, 20% of the system predissociates towards the $H_2+Fe(CO)_4$ (a^1B_2) primary products via tunneling through the potential energy barrier.

3.4. Dissociation on nonadiabatically coupled potentials

The diabatic time evolution of the $HMn(CO)_3(\alpha$-diimine) molecules on the three lowest coupled excited potentials $V^d_{a^3A'}$, $V^d_{b^3A'}$ and $V^d c^3A'$ (dashed lines labeled (1), (2) and (3) in Figs. 7 and 8) corresponding to the lowest MLCT ($d\rightarrow\pi^*$) and LLCT ($\sigma\rightarrow\pi^*$) excited states (σ being the bonding orbital between the metal center and the hydrogen, π^* being a vacant π orbital localized on the diimine ligand) is simulated by the time-dependent wave packet $\Psi_{a^3A'}(q_a,t)$ (q_a =[Mn–H]) solving the set of coupled time-dependent equations (Eq. (12)).
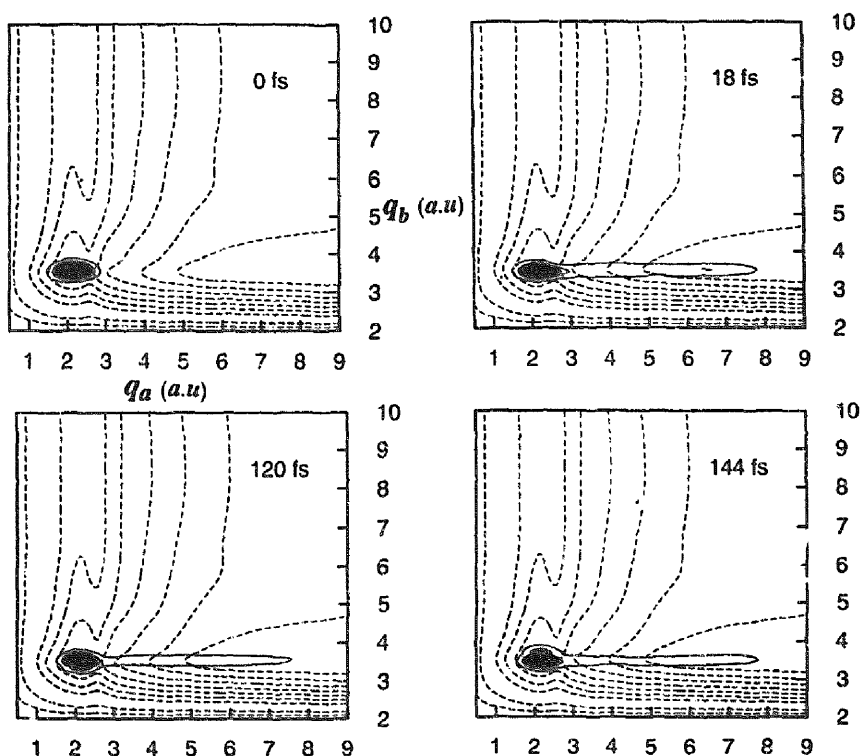
Fig. 6. Time evolution of the $\Psi_{a^1B_2}(q_a,q_b,t)$ wave packet on the $V_{a^1B_2}(q_a,q_b)$ PES of $H_2Fe(CO)_4(^1_aB_2)$, from the initial state $\Psi_{a^1B_2}(q_a,q_b,0) = |0,0\rangle_{a^1A_1}$ prepared by absorption $a^1A_1 \rightarrow a^1B_2$ [24].

The molecular reaction dynamics following absorption to the lowest ^{1}MLCT excited states (500 nm) and ^{1}MLCT→^{3}MLCT ISC is simulated with the initial conditions $\Psi_{a^3A'}(q_a,0) = |0,0\rangle_{a^1A'}$ and $\Psi_{b^3A'}(q_a,0) = \Psi_{c^3A'}(q_a,0) = 0$ and illustrated by the snapshots of the densities (Fig. 7). In an ultrafast time scale (within ca. 5 fs), about 20% of the initial wave packet is transferred to the upper bound ^{3}MLCT (b^{3}A′) and about 10% to the dissociative ^{3}LLCT (c^{3}A′) potential by the coupling which has its maximum in the ground state equilibrium region. The wave packet on the repulsive PEC dissociates towards the primary products H + Mn(CO)$_3$(α-diimine), whereas the main part gets trapped and oscillates into the ^{3}MLCT a^{3}A′ and b^{3}A′ bound potentials with exchange of amplitude among them.

High energy absorption in the 300 nm domain, brings the system in the singlet states corresponding to d→d or σ→π* excitations. The photodissociation dynamics following ISC to the ^{3}LLCT (c^{3}A′) dissociative potential is simulated by the time evolution of the $\Psi_{c^3A'}(q_a,t)$ (q_a =[Mn–H]), with the initial conditions $\Psi_{c^3A'}(q_a,0) = |0,0\rangle_{a^1A'}$ and $\Psi_{a^3A'}(q_a,0) = \Psi_{b^3A'}(q_a,0) = 0$ (Fig. 8). According to this second simulation, 90% of the wave packet dissociates towards the primary products H + Mn(CO)$_3$(α-diimine) within ca. 25 fs, whereas the rest of the molecules are

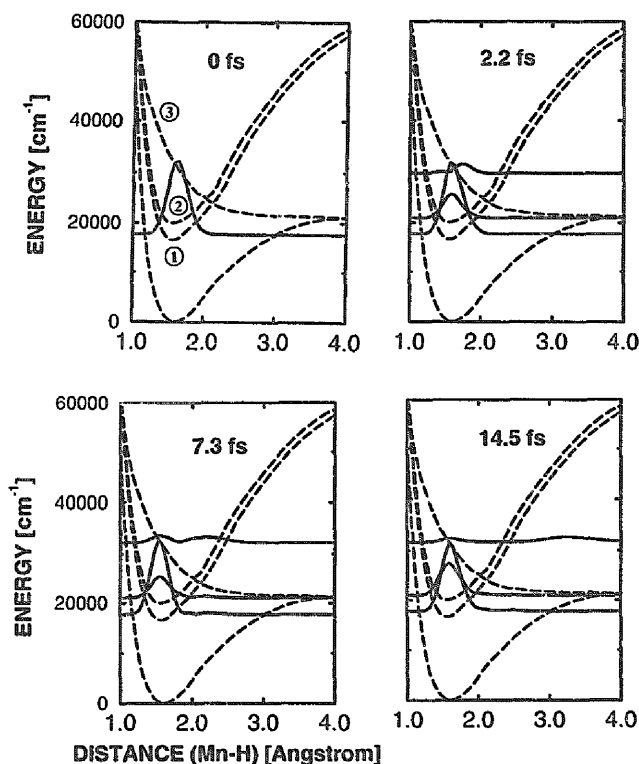Fig. 7. Diabatic time evolution of the $\Psi_{a^3A'}(q_a,t)$ wave packet (continuous line) on diabatically coupled $V^d_{a^3A'}(q_a)$, $V^d_{b^3A'}(q_a)$, and $V^d_{c^3A'}(q_a)$ PECs (dashed lines labeled (1), (2) and (3)) of HMn(CO)$_3$(α-diimine) with the initial conditions $\Psi_{b^3A'}(q_a,0)=\Psi_{c^3A'}(q_a,0)=0$ and the initial state $\Psi_{a^3A'}(q_a,0)=|0,0\rangle_{a^1A'}$ prepared by ISC.
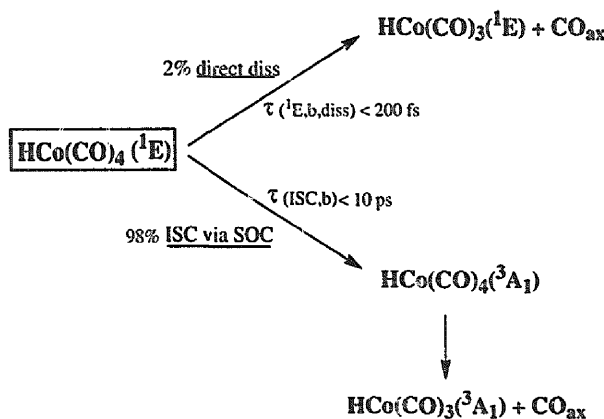
trapped within ca. 5 fs in the two lowest ^{3}MLCT potentials where they oscillate, mainly exchanging amplitude between them.

3.5. Radiationless spin–orbit coupled transitions

The molecular reaction dynamics of competing DD on the ^{1}E PES vs. indirect spin–orbit-induced dissociation on the ^{3}A$_1$ PES of the carbonyl axial ligand of HCo(CO)$_4$ is illustrated by the evolution of representative wavepackets $\Psi_{^1E}(q_b,t)$ resulting from solutions of the coupled Schrödinger equations (Eq. (12)) in the time domain $0 \leq t \leq 4000$ fs with the initial conditions $\Psi_{^1E}(q_b,0)=|0,0\rangle_{^1A_1}$ and $\Psi_{^3A_1}(q_b,0)=0$ ($q_b = [\text{Co-CO}_{ax}]$) (Fig. 9).

The probabilities $P(^1E)$ and $P(^3A_1)$ for observing HCo(CO)$_4$ in its ^{1}E and ^{3}A$_1$ states are shown in Fig. 10.

Other details, such as the separation of $P(e,b,t)$ into bound and dissociative parts or the autocorrelation function $\langle \psi_{^1E}(q_b,0)|\Psi_{^1E}(q_b,t)\rangle$ have enabled us to propose

$$HCo(CO)_3(^1E) + CO_{ax}$$

2% direct diss

$\tau\ (^1E,b,diss) < 200\ fs$

$$\boxed{HCo(CO)_4\ (^1E)}$$

$\tau\ (ISC,b) < 10\ ps$

98% ISC via SOC

$$HCo(CO)_4(^3A_1)$$

$$HCo(CO)_3(^3A_1) + CO_{ax}$$

Scheme 4.

the mechanism summarized in Scheme 4 for the spin–orbit induced $^1E \rightarrow {}^3A_1$ radiationless transition (ISC) along the Co–CO$_{ax}$ elongation in HCo(CO)$_4$ [41].

3.6. Mode selective control of unimolecular dissociation by a two-photon laser strategy

In order to demonstrate the Polanyi rules for unimolecular reactions, the photodissociation of HCo(CO)$_4$(^1E, d$\rightarrow\sigma^*$) (the reaction in Eq. (2)) is simulated starting from two different preparations of initial vibrational states $|v_a, v_b\rangle$. As reference, we consider the time evolution of the $\Psi_{^1E}(q_a, q_b, t)$ wave packet ($q_a =$[Co–H], $q_b =$[Co–CO$_{ax}$]), illustrated in Fig. 3 with the initial wavefunction $\Psi_{^1E}(q_a, q_b, t=0)$ $=|0,0\rangle_{^1A_1}$. The 'femtochemical' branching ratio [H+Co(CO)$_4$]/ [HCo(CO)$_4$(^1E,IVR)]$\cong$0.35/0.65 has been determined from the autocorrelation function $\langle\Psi_{^1E}(q_a, q_b, 0)|\Psi_{^1E}(q_a, q_b, t)\rangle$. The effect of the investment of two quanta of energy into the bond $q_a =$[Co–H], the bond to be broken, is illustrated by the time evolution of the initial wave packet $\Psi_{^1E}(q_a, q_b, t=0)=|2,0\rangle_{^1A_1}$ on the ^1E potential (Fig. 11).

Already, two vibrational quanta in bond q_a invert the branching ratio in favor of the Co–H homolysis instead of IVR, giving now a 'femtochemical' branching ratio of [H+Co(CO)$_4$]/[HCo(CO)$_4$(^1E,IVR)]$\cong$0.98/0.02. The wavefunction $\Psi_{^1E}(q_a, q_b, t)$ proves to be almost completely dissociative, implying perfect control of the reaction in Eq. (2):
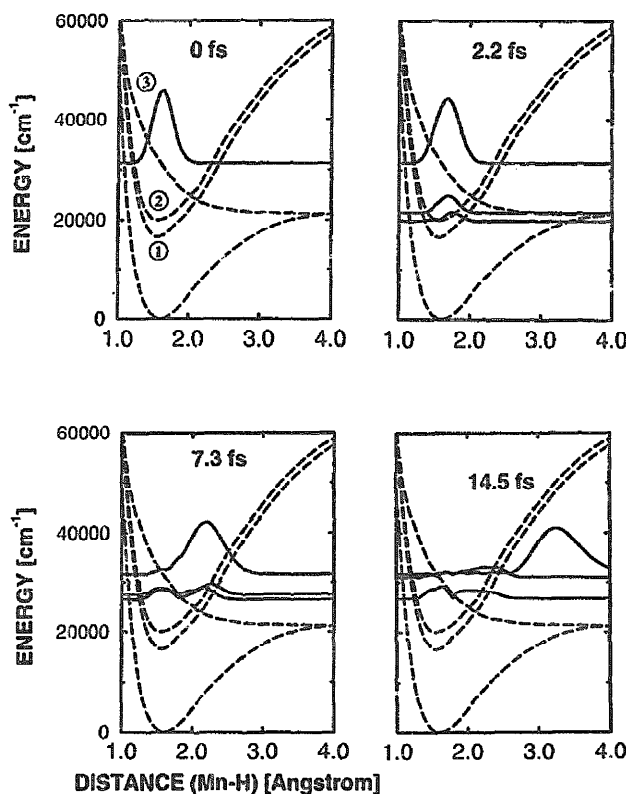
$$HCo(CO)_4(^1A_1) \xrightarrow{h\nu} [HCo(CO)_4]^*(^1E)$$

$$[H+Co(CO)_4]^*(^1E)$$

diss

$$[HCo(CO)_4]^*(^1E)$$

IVR

$$HCo(CO)_4(^1E)$$
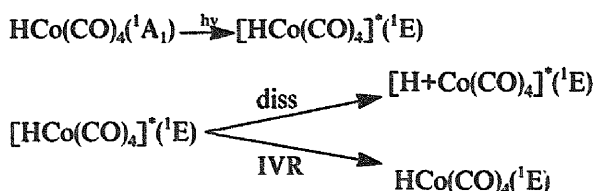
Fig. 8. Diabatic time evolution of the $\Psi_{c^3A_r}(q_a,t)$ wave packet on diabatically coupled $V^d_{a^3A_r}(q_a)$, $V^d_{b^3A_r}(q_a)$, and $V^d_{c^3A_r}(q_a)$ PECs (dashed lines labeled (1), (2) and (3)) of HMn(CO)$_3$(α-diimine) with the initial conditions $\Psi_{a^3A_r}(q_a,0) = \Psi_{b^3A_r}(q_a,0) = 0$ and the initial state $\Psi_{c^3A_r}(q_a,0) = |0,0\rangle_{a^1A_r}$ prepared by ISC.

3.7. Absorption spectra

3.7.1. Absorption spectrum of HCo(CO)$_4$

The Fourier transform of the $\langle \Psi_{^1E}(0)|\Psi_{^1E}(t)\rangle$ autocorrelation function represented in Fig. 4 and illustrating the decay of the $\Psi_{^1E}(q_a,q_b,t=0) = |0,0\rangle_{^1A_1}$ initial wave packet on the ^1E potential, initially populated after irradiation of HCo(CO)$_4$ at 254 nm, results in the absorption spectrum (Fig. 12) for cw excitation in the Franck–Condon regime of the $^1A_1 \rightarrow {}^1E$ allowed transition:

$$I\left({}^1A_1 \rightarrow {}^1E, \omega\right) \propto \int_{-\infty}^{\infty} dt\, e^{+i(E^1A_{1,0} + \hbar\omega)t/\hbar} \left\langle \Psi_{^1E}(t=0) \middle| \Psi_{^1E}(t) \right\rangle \tag{13}$$

where $E^1A_{1,0}$ is the energy of the initial state, and ω is the absorption frequency.

The absorption spectrum exhibits two contributions from product channels α corresponding to the formation of the primary products H + Co(CO)$_4$ in the ^1E excited state plus β corresponding to the IVR process of HCo(CO)$_4$(^1E). This
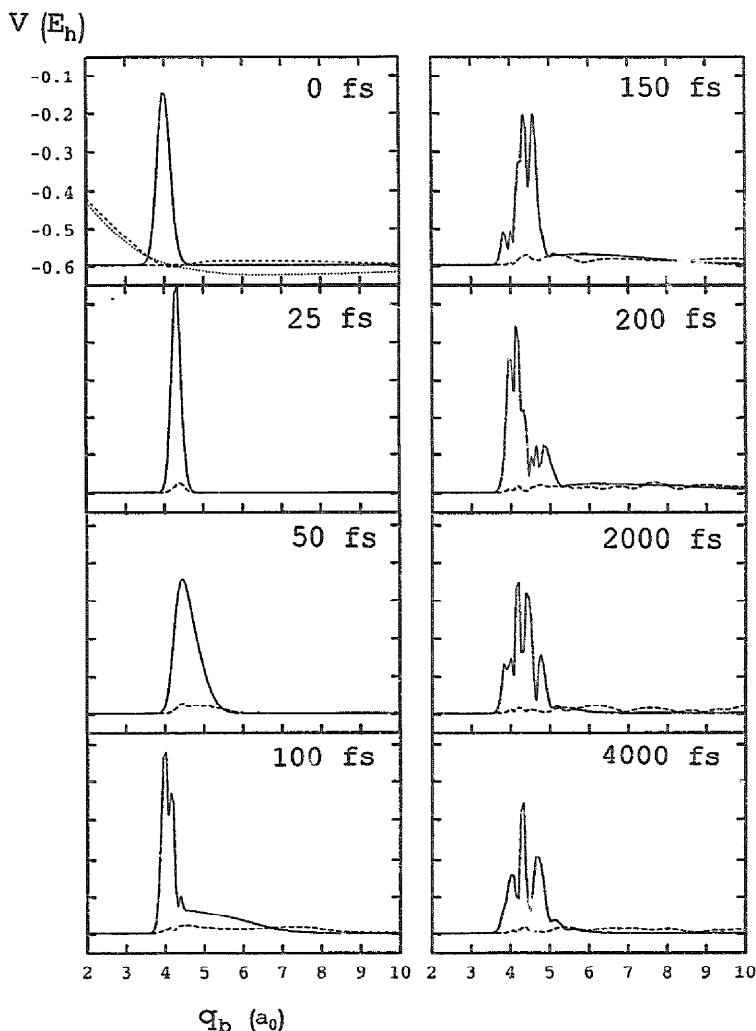
Fig. 9. Time evolution of the $\Psi_{^1E}(q_b,t)$ (continuous line) and $\Psi_{^3A_1}(q_b,t)$ (dashed line) wave packets on the spin–orbit coupled potentials $V_{^1E}(q_b)$ and $V_{^3A_1}(q_b)$ (dashed and dotted lines in snapshots 1, $t=0$ fs) PECs of HCo(CO)$_4$ in the time domain 0–4000 fs.

spectrum is characterized by three important features: (i) a very strong peak at $\lambda=229.8$ nm; (ii) a medium peak at $\lambda=210.9$ nm; (iii) a broad, small peak, which appears as a shoulder of the medium peak, extending until $\lambda=185$ nm. The decomposition of the spectrum into two parts related to channels α and β shows that the two peaks at $\lambda=229.8$ nm and $\lambda=210.9$ nm are due to excitation of IVR of HCo(CO)$_4$(^1E); more specifically, the strong peak at $\lambda=229.8$ nm arises from the dominant vibrational excitation CO–CO$_{ax}$, which causes the prominent oscillations of the autocorrelation function at time $t>10$ fs; the medium peak is due to excitation
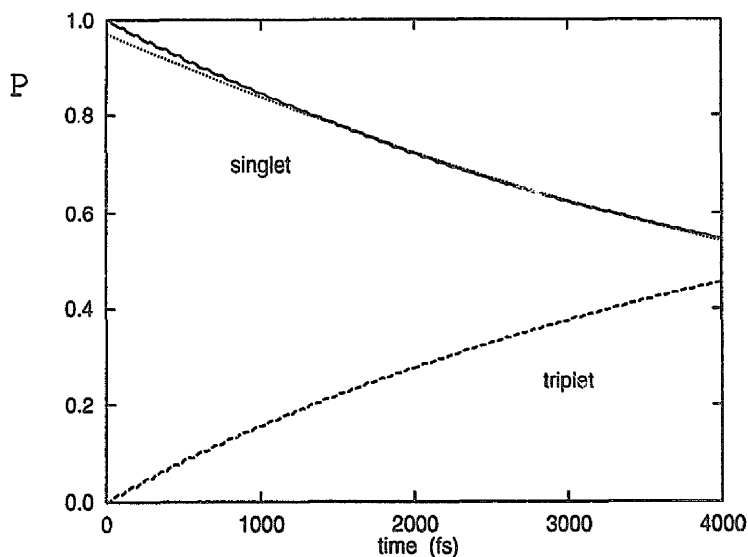
Fig. 10. ISC $^1E \rightarrow {}^3A_1$ in $HCo(CO)_4$, induced by $Co-CO_{ax}$ vibrations. The probabilities $P(^1E)$ and $P(^3A_1)$ for observing $HCo(CO)_4$ in its ^1E and $^3A_1$ states are shown by continuous and dashed lines respectively.

of Co–H vibrations. The long tail of the spectrum until 185 nm is due to the channel α corresponding to the homolysis of the Co–H bond. If the comparison with the experimental spectrum [22] yields good agreement for the intense band at $\lambda = 227$ nm (calculated at 229.8 nm), for which there is no doubt experimentally, the other details do not allow any correlation. Indeed, the comparison with the experimental spectrum at higher energies is featureless, since the detection is close to the lower wavelength limit of the spectrometer.

3.7.2. Absorption spectrum of $H_2Fe(CO)_4$

The total absorption spectrum of $H_2Fe(CO)_4$ obtained by the sum over the individual contributions of the three lowest a^1B_1, a^1B_2 and b^1A_1 excited states weighted by their transition dipole moments is represented in Fig. 13.

The theoretical spectrum is characterized by two bands in the energy domain between 227 and 294 nm in rather good agreement with the experimental spectrum [6a] which shows an absorption shoulder between 240 and 290 nm and with the wavelength of irradiation (254 nm) responsible for molecular hydrogen elimination. The contributions of the two a^1B_1 and b^1A_1 singlet excited states is illustrated by two broad absorption bands with their maxima at 274 nm and 245 nm respectively, reflecting the total DD processes on the corresponding potentials. The a^1B_2 $(d \rightarrow \sigma_u^*)$ excited state has no significant contribution to the theoretical absorption spectrum owing to its low dipole transition moment.
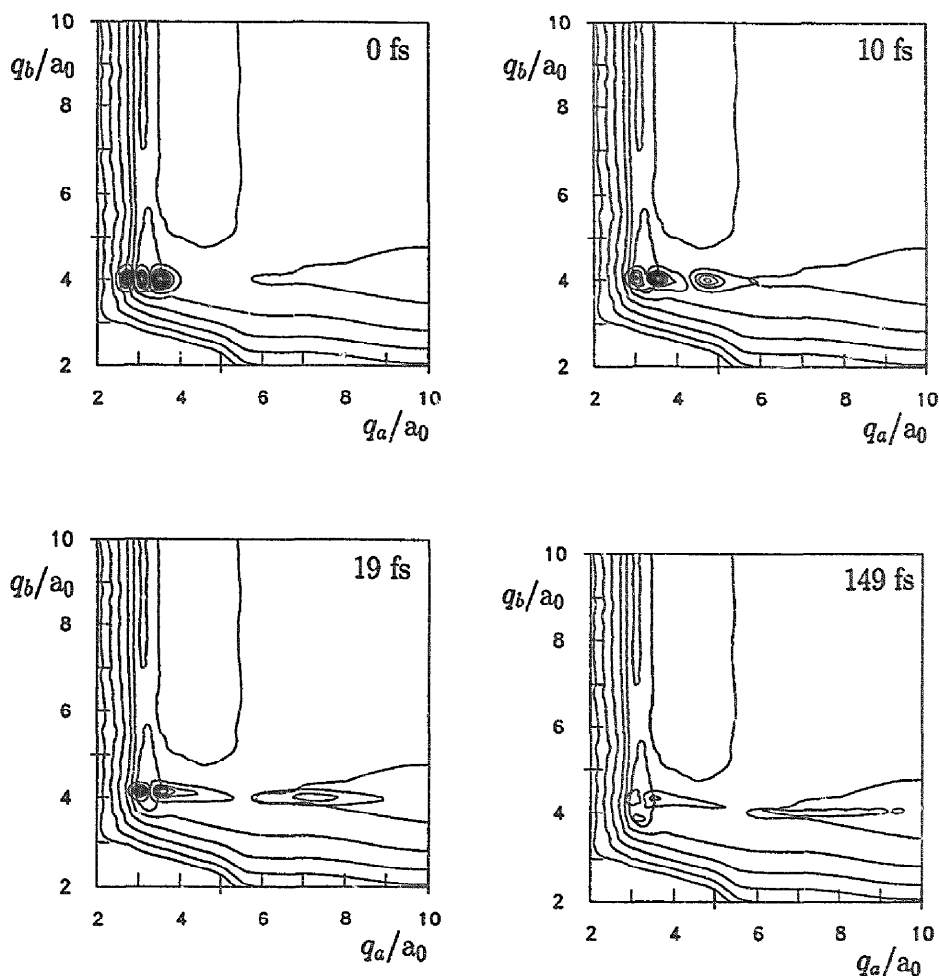
Fig. 11. Time evolution of the $\Psi_{^1E}(q_a,q_b,t)$ wave packet on the $V_{^1E}(q_a,q_b,t)$ PES of HCo(CO)$_4$(^{1}E) from the initial state $\Psi_{^1E}(q_a,q_b,0) = |2,0\rangle_{^1A_1}$ prepared by a two-photon laser IR + UV strategy.

4. Conclusion

From the results reported above, it seems clear that quantum calculations coupled with dynamics simulation can contribute significantly to the understanding of photo-chemical reactions in organometallics. An analysis of the dynamics of the elementary processes which contribute to the photodissociation has enabled us to determine without ambiguity the nature of the photoactive excited states, the time scales, the branching ratio of the primary reactions, and some important features of the absorption spectra. Mode selective control of unimolecular dissociation by a two-photon laser strategy, as well as dissociation on coupled potentials, either kinetically or by spin–orbit interaction, have been reported.
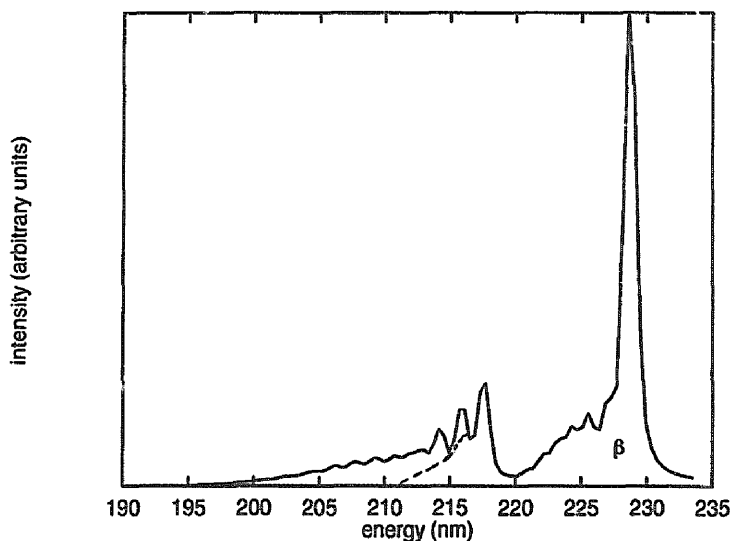
Fig. 12. Simulated total (t) absorption spectra $I(^1A_1 \rightarrow {}^1E,\omega) = I(^1A_1 \rightarrow {}^1E,\alpha,\omega) + I(^1A_1 \rightarrow {}^1E,\beta,\omega)$ with contributions from two competing product channels α (dissociation toward the products $H + Co(CO)_4(^1E)$) and β (IVR of $HCo(CO)_4(^1E)$).
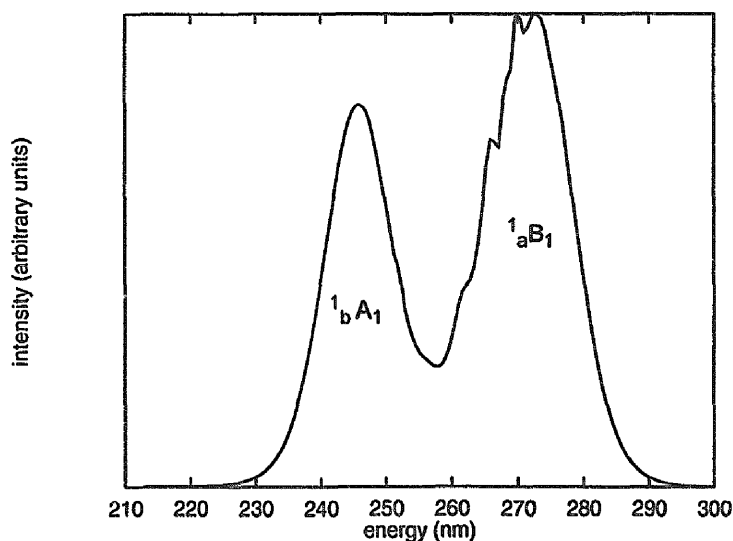

Fig. 13. Simulated total (t) absorption spectra $I(a^1A_1 \rightarrow a^1B_1,\omega) + I(a^1A_1 \rightarrow a^1B_2) + I(a^1A_1 \rightarrow b^1A_1,\omega)$.

Further work will need more accurate multidimensional PESs taking into account relaxation phenomena and solvent effects in electronic excited states. Fast time-resolved spectroscopy (beyond the picosecond time scale) has also to be developed in order to reduce the gap between experiments and numerical simulations.

References

[1] M.D. Likar, J.E. Baggot, A. Sinha, T.M. Ticih, R.L. Vander Wal and F.F. Crim, J. Chem. Soc. Faraday Trans. 2:, 84 (1988) 1483; F.F. Crim, Science, 249 (1990) 1387; P.F. Zittle and V.I. Lang, J. Photochem. Photobiol. A:, 56 (1991) 149; R. Schinke, Photodissociation Dynamics, Cambridge University Press, Cambridge, 1993; S.K. Kim, S. Pedersen and A.H. Zewail, Chem. Phys. Lett., 233 (1995) 500; T. Baumert, S. Pedersen and A.H. Zewail, J. Phys. Chem., 97 (48) (1993) 12447; S. Pedersen, T. Baumert and A.H. Zewail, J. Phys. Chem., 97 (48) (1993) 12460 and references cited therein.
[2] E. Segev and M. Shapiro, J. Chem. Phys., 73 (1980) 2001; 77 (1982) 5604; R. Schinke, V. Engel and V. Staemmler, J. Chem. Phys., 83 (1985) 4522; V. Engel, R. Schinke and V. Staemmler, J. Chem. Phys., 88 (1988) 129.
[3] J. Zhang and D.G. Imre, Chem. Phys. Lett., 149 (1988) 233; J. Zhang, D.G. Imre and J.H. Frederick, J. Phys. Chem., 93 (1989) 1840; D. Chasman, D.G. Imre and D.J. Tannor, J. Chem. Phys., 89 (1988) 6667; D.G. Imre and J. Zhang, J. Chem. Phys., 139 (1989) 89; J. Zhang, E.J. Heller, D. Huber, D.G. Imre and D.J. Tannor, J. Chem. Phys., 89 (1988) 3602; S. Das and D.J. Tannor, J. Chem. Phys., 91 (1989) 2324.
[4] G.L. Wrighton and J.R. Lehman, Adv. Inorg. Chem. Radiochem., 20 (1977) 189; G.L. Geoffroy and M.S. Wrighton, Organometallic Chemistry, Academic Press, New York, 1979; G.L. Geoffroy, Prog. Inorg. Chem., 27 (1980) 123.
[5] J.J. Turner, in E. Kochanski (ed.), Photoprocesses in Transition Metal Complexes, Biosystems and other Molecules: Experiments and Theory, NATO ASI Series C, Vol. 376, 1992, pp. 113–140; F.W. Grevels, in E. Kochanski (ed.), Photoprocesses in Transition Metal Complexes, Biosystems and other Molecules: Experiments and Theory, NATO ASI Series C, Vol. 376, 1992, pp. 141–171.
[6] (a) R.L. Sweany, in A. Dedieu (ed.), Transition Metal Hydrides, VCH, New York, 1991 pp. 65–101. (b) M. Poliakoff and E. Weitz, Adv. Organomet. Chem., 25 (1986) 277.
[7] K.A. Singmaster, F.A. Houle and R.J. Wilson, J. Phys. Chem., 94 (1990) 6864; J.M. Parnis, S.A. Mitchell and P.A. Hackett, J. Phys. Chem., 94 (1990) 8152; S. Niles, D.A. Prinslow, C.A. Wight and P.B. Armentrout, J. Chem. Phys., 93 (1990) 6186; W.E. Hollingworth and V. Vaida, J. Chem. Phys., 90 (1986) 1235; W.R. Pfeifer and J.F. Garvey, J. Chem. Phys., 93 (1989) 5906.

[8] K. Kalyanusundaram, Coord. Chem. Rev., 46 (1982) 159; T.J. Meyer, Pure Appl. Chem., 58 (1986) 1193; T.J. Meyer, Acc. Chem. Res., 22 (1989) 163.

[9] A. Juris, V. Balzani, F. Barigelletti, S. Campagna, P. Belser and A. Von Zelewsky, Coord. Chem. Rev., 84 (1988) 85; E. Krausz and J. Ferguson, Prog. Inorg. Chem., 37 (1989) 293; D.J. Stufkens, Comments Inorg. Chem., 13 (1992) 359.

[10] V. Balzani, L. De Cola, L. Prodi and F. Scandola, Pure Appl. Chem., 62 (1990) 1457; F. Scandola, C.A. Bignozzi, C. Chiorboli, M.T. Indelli and M.A. Rampi, Coord. Chem. Rev., 97 (1990) 299; A. Juris, S. Campagna, I. Bidd, J.M. Lehn and R. Ziessel, Inorg. Chem., 27 (1988) 40007.

[11] H. Hermann, F.W. Grevels, A. Henne and K. Schaffner, J. Phys. Chem., 86 (1982) 5156.

[12] J.N. Moore, P.A. Hansen and R.M. Hochstrasser, Chem. Phys. Lett., 138 (1987) 110; J. Am. Chem. Soc., 111 (1989) 4563; P.A. Anfinrud, C.H. Han, T. Lian and R.M. Hochstrasser, J. Phys. Chem., 95 (1991) 574; L. Wang, X. Zhu and K.G. Spears, J. Am. Chem. Soc., 110 (1988) 8695; J. Phys. Chem., 93 (1989) 2.

[13] C. Daniel, M.C. Heitz, L. Lehr, J. Manz and T. Schröder, J. Phys. Chem., 97 (1993) 12485.

[14] C. Daniel, E. Kolba, L. Lehr, J. Manz and T. Schröder J. Phys. Chem., 98 (1994) 9823.

[15] C. Daniel, M.C. Heitz, L. Lehr, T. Schröder and B. Warmuth, Int. J. Quant. Chem., 52 (1994) 71.

[16] C. Daniel, R. De Vivie-Riedle, M.C. Heitz, J. Manz and P. Saalfrank, Int. J. Quant. Chem., 57 (1996) 595.

[17] A. Veillard and A. Strich, J. Am. Chem. Soc., 110 (1988) 3793; C. Daniel, J. Am. Chem. Soc., 114 (1992) 1625; C. Daniel, Coord. Chem. Rev., 97 (1990) 141.

[18] C. Daniel and A. Veillard, in A. Dedieu (ed.), Transition Metal Hydrides, VCH, New York, 1991, pp. 235–261; C. Daniel, J. Phys. Chem., 95 (1991) 2394.

[19] M.M. Rohmer and A. Veillard, New J. Chem., 15 (10) (1991) 795; A. Veillard and A. Dedieu, New J. Chem., 7 (12) (1983) 683.

[20] K. Finger and C. Daniel, J. Chem. Soc. Chem. Commun., (1995) 1427; K. Finger and C. Daniel, J. Am. Chem. Soc., 117 (1995) 12322.

[21] R.L. Sweany, Inorg. Chem., 19 (1980) 3512.

[22] R.L. Sweany, Inorg. Chem., 21 (1982) 752.

[23] R.L. Sweany, J. Am. Chem. Soc., 104 (1982) 3739.

[24] M.C. Heitz and C. Daniel, Proc. 54th Int. Meet. of Physical Chemistry, Lille, France, 1995; M.C. Heitz and C. Daniel, J. Am. Chem. Soc., submitted; M.C. Heitz and C. Daniel, Chem. Phys. Lett., 246 (1995) 488.

[25] R.L. Sweany, J. Am. Chem. Soc., 103 (1981) 2410.

[26] D.J. Stufkens, Coord. Chem. Rev., 104 (1990) 39; M.W. Kokkes, T.L. Snoeck, D.J. Stufkens, A. Oskam, M. Christophensen and C.H. Stam, J. Mol. Struct., 13 (1985) 11.

[27] R.W. Balk, T.L. Snoeck, D.J. Stufkens and A. Oskam, Inorg. Chem., 19 (1980) 3015.

[28] H.V. Van Dijk, D.J. Stufkens and A. Oskam, J. Am. Chem. Soc., 111 (1989) 541.

[29] P.C. Servaas, D.J. Stufkens and A. Oskam, Inorg. Chem., 28 (1989) 178.

[30] G.J. Stor, S.L. Morisson, D.J. Stufkens and A. Oskam, Organometallics, 13 (1994) 2641.

[31] T.J. Meyer and V. Caspar, Chem. Rev., 85 (1985) 187.

[32] B.D. Rossenaar, C.J. Kleverlaan, D.J. Stufkens and A. Oskam, J. Chem. Soc. Chem. Commun., (1994) 63.

[33] B.D. Rossenaar, T. Van der Graaf, R. Van Eldik, C.H. Langford, D.J. Stufkens and A. Vleck, Jr., Inorg. Chem., 33 (1994) 2865.

[34] G. Stor, D.J. Stufkens, P. Vernooijs, E.J. Baerends, J. Fraanje and K. Goubitz, Inorg. Chem., 34 (1995) 1588.

[35] B.R. Johnson and J.L. Kinsey, J. Chem. Phys., 91 (1989) 7638; E.J. Heller, Acc. Chem. Res., 14 (1981) 368; S.Y. Lee and E.J. Heller, J. Chem. Phys., 76 (1982) 3035; E.J. Heller, R.L. Sundberg and D.J. Tannor, J. Phys. Chem., 86 (1982) 1822.

[36] J.E. Combariza, C. Daniel, B. Just, E. Kades, E. Kolba, J. Manz, W. Malisch, G.K. Paramonov and B. Warmuth, in J.A. Kaye (ed.), Isotope Effects in Gas Phase Chemistry, ACS Symposium Series 502, American Chemical Society, Washington, DC, 1992, Chapter 20, p. 310.

[37] M. Shapiro and R. Bersohn, J. Chem. Phys., 73 (1980) 3810; M. Shapiro, Chem. Phys. Lett., 81

(1981) 521; M. Shapiro, J. Phys. Chem., 90 (1986) 3644; B. Hartke, J. Manz and J. Mathis, J. Chem. Phys., 139 (1989) 123.

[38] H. Tal-Ezer and R. Kosloff, J. Chem. Phys., 81 (1984) 3967; R. Kosloff and H. Tal-Ezer, Chem. Phys. Lett., 127 (1986) 223.

[39] R. Kosloff and D. Kosloff, J. Chem. Phys., 79 (1983) 1823; D. Kosloff and R. Kosloff, J. Comput. Phys., 52 (1983) 35; R. Kosloff and D. Kosloff, J. Comput. Phys., 631 (1986) 363.

[40] K. Finger, C. Daniel, P. Saalfrank and B. Schmid, J. Phys. Chem., 100 (1996) 3368; M.C. Heitz, C. Ribbing and C. Daniel, J. Chem. Phys., 106(4) (1997) 1421.

[41] C. Daniel, M.C. Heitz, J. Manz and C. Ribbing, J. Chem. Phys., 102 (2) (1995) 905.

[42] C. Ribbing and C. Daniel., J. Chem. Phys., 100 (1994) 6591.

[43] F.T. Smith, Phys. Rev., 179 (1969) 111.

[44] G. Hirsch, P.J. Bruna, R.J. Buenker and S.D. Peyerimhoff, Chem. Phys., 45 (1980) 335.